

Visible Cone-Beam Tomography With a Lensless Interferometric Camera

Daniel L. Marks,^{1,2} Ronald A. Stack,¹ David J. Brady,^{1,2*}
David C. Munson Jr.,^{1,2} Rachael B. Brady³

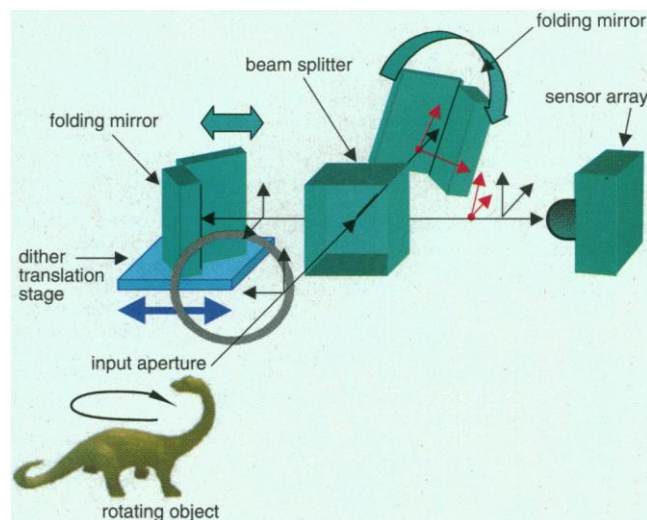
Digital processing of optical coherence functions can reconstruct three-dimensional objects illuminated by incoherent light. It is shown that Fourier analysis of the mutual intensity of the field produces projections that are mathematically identical to the projections of x-ray cone-beam tomography. A lensless interferometric camera that captures planes of mutual intensity data is described and used to reconstruct an incoherently illuminated visible object in three dimensions.

Lenses act as analog computers that transform the incident field into an image of the field in a particular plane. With the continuing digital revolution, one may wonder whether this analog processing can be digitally enhanced. This report describes digital imaging with an optical system consisting only of smooth planar surfaces. As is often the case when a digital processor replaces an analog one, our motivation is to improve the analog algorithm. The improvement we obtain is infinite depth of focus, which is equivalent to the geometrical optics assumption that the field propagates in nondiffracting rays. This assumption is satisfactory in medical x-ray tomography because one is satisfied to resolve features that are large compared with the wavelength of the illuminating radiation. With visible imaging, one often wishes to resolve features as close to the wavelength scale as possible, in which case diffraction cannot be neglected. Here we show that visible ray projection data obtained from digital analysis of interferometric data can be combined with tomographic algorithms to reconstruct three-dimensional (3D) objects. Our results show that neither point-by-point scanning, as in confocal microscopy or coherence tomography, nor heuristic analysis, as in computer vision, is necessary for 3D reconstruction and that diffraction-limited 3D optical reconstruction is possible from purely physical field analysis.

We obtained infinite depth of focus images by digital analysis of the mutual intensity function. For quasi-monochromatic light, the mutual intensity between two points is $J_{12} = \langle E_1 E_2^* \rangle$, where $\langle \rangle$ is the statistical expected value. E_1 and E_2 are the complex field values at points 1 and 2, and we considered scalar fields for sim-

plicity (I). If the field arises from a primary source in free space, its value at point 1 is a superposition of Huygens wavelets. This superposition can be expressed as $E_1 = \int E_s (e^{jkR_{1s}}/R_{1s}) d^3r_s$, where j represents $\sqrt{-1}$, E_s is the source field density, $k = 2\pi/\lambda$, and position vector r_s is the variable of integration. The integral is over the source volume, and R_{1s} is the distance from a source point to point 1. For a spatially incoherent source, $\langle E_s E_{s'}^* \rangle = I_s \delta(\mathbf{r}_s - \mathbf{r}_{s'})$, where I_s is the source intensity density due to the field fluctuations E_s and $E_{s'}$ at points \mathbf{r}_s and $\mathbf{r}_{s'}$, respectively, and $\delta(\cdot)$ is the Dirac delta function. After double integrations over \mathbf{r}_s and $\mathbf{r}_{s'}$, the expectation reduces to $J_{12} = \int I_s (e^{jk(R_{1s}-R_{2s})}/R_{1s}R_{2s}) d^3r_s$. Interferometric astronomical imaging uses a far-field approximation of this integral in which the source space reduces to 2D and the exponential term becomes a Fourier transform kernel (2, 3). The integral can be inverted to obtain the 3D source density with Fourier or modal methods (4-8). High depth of focus has been studied in the context of statistical radiometry (9).

Fig. 1. The rotational shear interferometer (RSI) is a two-arm Michelson-style interferometer. A folding mirror consisting of a pair of planar mirrors joined at right angles terminates each arm. Each folding mirror inverts the incident field across its axis. The RSI measures planes of interference data in parallel with an electronic sensor array in the output aperture. The folding mirrors are nominally placed so that the optical path difference between the arms is zero. The interference is separated from background terms by dithering the relative optical path delay with a translation stage on one arm. The coordinate system of the object corresponds to (x_s, y_s, z_s) , and the plane of the sensor array corresponds to the correlation space $(\Delta x, \Delta y)$.



To use the mutual intensity to obtain cone-beam projections, we assumed that source point \mathbf{r}_s was confined to a semiinfinite region $z_s > 0$ with Cartesian coordinates (x_s, y_s, z_s) and the coherence sampling points (for example, points 1 and 2) were confined to a planar aperture on $z_s = 0$. We chose the origin of the aperture at the midpoint between the two sampling points and defined Δx and Δy to be the distance between the sampling points along the x and y axes. The Cartesian coordinates of the sampling points are $(\Delta x/2, \Delta y/2, 0)$ and $(-\Delta x/2, -\Delta y/2, 0)$. Finally, we made the paraxial approximation that $z_s \gg \Delta x, \Delta y, x_s, y_s$ for all points in the source volume and in the correlation aperture. This implies that $R_{1s} \approx z_s + [(\Delta x/2 - x_s)^2 + (\Delta y/2 - y_s)^2]/2z_s$ and $R_{2s} \approx z_s + [(\Delta x/2 + x_s)^2 + (\Delta y/2 + y_s)^2]/2z_s$. Under this approximation,

$$J(\Delta x, \Delta y) =$$

$$\int \frac{I_s}{z_s^2} \exp\left[-\frac{j2\pi}{\lambda z_s} (x_s \Delta x + y_s \Delta y)\right] d^3r_s \quad (1)$$

where λ is the center wavelength of the source. Taking the inverse Fourier transform



Fig. 2. Photograph of the test object. The maximal length of the object is 7.2 cm, the width is 2.1 cm, and the height is 4.9 cm.

¹Beckman Institute for Advanced Science and Technology, ²Department of Electrical and Computer Engineering, ³National Center for Supercomputing Applications, University of Illinois at Urbana-Champaign, 405 North Mathews Avenue, Urbana, IL 61801, USA.

*To whom correspondence should be addressed. E-mail: dbrady@uiuc.edu

REPORTS

of Eq. 1 with respect to Δx and Δy , we obtained

$$\begin{aligned} \tilde{J}(u, v) &= \\ &= \int J(\Delta x, \Delta y) \exp[j2\pi(u\Delta x + v\Delta y)] d\Delta x d\Delta y \\ &= \int \frac{I_s}{z_s^2} \delta\left(u - \frac{x_s}{\lambda z_s}, v - \frac{y_s}{\lambda z_s}\right) d^3 r_s \end{aligned} \quad (2)$$

$\tilde{J}(u, v)$ is a line integral through I_s/z_s^2 along a ray passing through the points $(x_s = \lambda z_s u, y_s = \lambda z_s v, z_s)$. Values of $\tilde{J}(u, v)$ for all allowed values of u and v correspond to integrals along a cone of rays diverging from the vertex point $(x_s = y_s = z_s = 0)$. In x-ray tomography, a cone of projection data is gathered by placing a planar sensor on the opposite side of the object volume from a point source. Equation 2 shows that a mathematically equivalent cone of data for a self-luminous or ambiently illuminated visible object is obtained by measuring the mutual intensity on a plane centered on the equivalent (but now virtual) point source.

Planes of mutual intensity data may be measured in parallel with a rotational shear interferometer (RSI) (Fig. 1) (10–13). We obtained experimental data using an RSI formed of a 5-cm aperture beam splitter and 5-cm folding mirrors. One of the folding mirrors was mounted on a piezo-driven flexure stage to vary the optical path length. The only other elements in the optical system were a mechanical shutter at the RSI input, a 3-nm bandpass spectral filter centered on a wavelength of 633 nm at the output plane, and a 512 pixel by 512 pixel back-illuminated charge-coupled device (CCD) detector array. The spectral filter enforces the quasi-monochromatic assumption. For a quasi-monochromatic field, an RSI isolates the amplitude and phase of the mutual intensity by sampling the output plane intensity as a function of optical path difference. We measured the output for eight optical path delays between the two

arms. The eight delays are evenly spaced over one wavelength of maximal relative delay. The discrete Fourier transform of the intensity image over these eight frames is $J(\Delta x, \Delta y)$.

Cone-beam tomography uses ray projections through vertices lying on a curve called the vertex path. Exact reconstruction of an object volume is possible if all planes through the object volume intersect the vertex path (14). Vertex paths that sample incomplete data are often used for implementation simplicity. We used an algorithm from Feldkamp *et al.* (15) in our experiments. This algorithm is based on a circular vertex path. Our test object (Fig. 2) was placed 1.61 m from the RSI sensor plane and illuminated by a white halogen lamp. We sampled a circular vertex path by rotating the object in front of the RSI. Planes of coherence data were recorded from 128 vertex points equally spaced in angle over one revolution. At each vertex point, we captured eight frames of 128 by 128 intensity samples. These frames were demodulated to estimate $J(\Delta x, \Delta y)$, which was then Fourier transformed to obtain 128 planes of $\tilde{J}(u, v)$ data. These planes were used in the cone-beam algorithm to reconstruct the 128 by 128 by 128 data volume (Fig. 3). The reconstructed data cube is 10.6 cm on a side with a resolution of 830 μm . The object size and resolution are determined by the range and sampling rate of $(\Delta x, \Delta y)$. The sampling rate was the CCD pixel spacing (22 μm), and the range was limited by the RSI aperture (limited by the CCD array size to 0.63 cm) and by the angle between the fold axes (6.55°) to 0.7 mm (16).

Our derivation assumes that the object is translucent, but our experiment reconstructs an opaque object. Opacity has surprisingly little effect for objects without occluding surfaces. The tomographic reconstruction of a convex opaque object is a linear superposition of the reconstructions of the differential surface patches that make up the object. The opacity of each surface patch can be modeled as a window on the solid angle over which the patch radiates.

The window function produces a characteristic patch response oriented according to the patch's surface normal (Fig. 4). For a convex object, the reconstruction is the convolution of the surface with the patch response function. In the nonconvex case, surface patches may obscure each other, resulting in the reconstruction no longer being a unique function of the surface structure. The volume surrounding the feet of the object reported here is nonconvex, which leads to uncertainty in the reconstruction of this region (Fig. 5).

Systems combining digital computation with a coherence sensor such as the RSI can achieve infinite depth of field. This property makes cone-beam tomography a flexible tool to synthesize 3D structure from coherence information. Such physical optics techniques may ultimately benefit microscopy and machine vision by providing 3D reconstructions of supe-

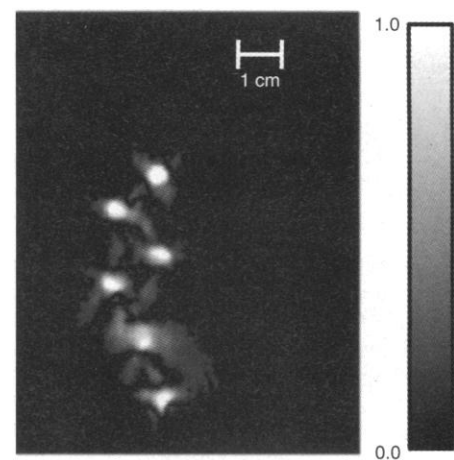
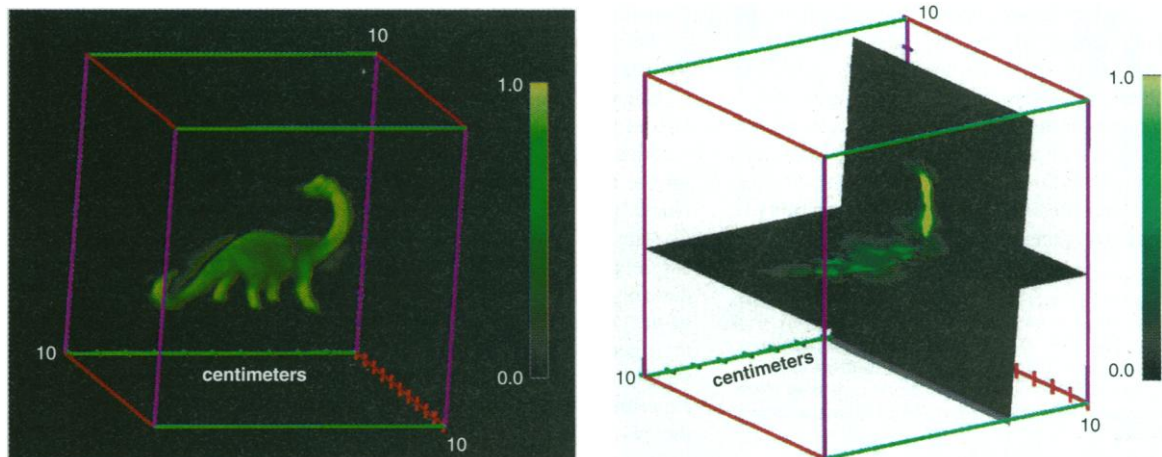


Fig. 5. Slice $z = 84$ of the data volume showing the legs, the tail going down, and the tail coming up. The four top white circles are cross sections of the legs and the bottom two circles are cross sections of the tail. The "fill" between the legs and around the tail is due to the angular windowing resulting from occlusion of some patches.

Fig. 3 (left). A pseudo-color volume rendering of the 128 by 128 by 128 reconstructed data volume. The haze around the reconstructed data volume in Fig. 3 is due to the spatial distribution of the patch response function. **Fig. 4 (right).** The data volume with planes slicing the neck and body of the dinosaur. The brightness on the planes corresponds to the reconstructed intensity density. The spatial distribution of the patch response function is readily visible on the body slice.



rior resolution. Nonimaging sensors may provide advantages over lens-based cameras, because our knowledge of the environment should be limited by the information available from it and not our sensing or computational methods, analog or digital.

References and Notes

1. L. Mandel and E. Wolf, *Optical Coherence and Quantum Optics* (Cambridge Univ. Press, Cambridge, 1995).
 2. C. V. Schooneveld, Ed., *Image Formation from Coher-*

ence Functions in Astronomy, IAU Colloquium no. 49 (Reidel, Groningen, Netherlands, 1978), vol. 76.
 3. G. W. Swenson, *J. Opt. Soc. Am. A* **3**, 1311 (1986).
 4. W. H. Carter and E. Wolf, *Opt. Acta* **28**, 227 (1981).
 5. A. J. Devaney, *J. Math. Phys.* **20**, 1687 (1979).
 6. I. J. LaHaie, *J. Opt. Soc. Am. A* **2**, 35 (1985).
 7. J. Rosen and A. Yariv, *Opt. Lett.* **21**, 1803 (1996).
 8. A. M. Zarubin, *Opt. Commun.* **100**, 491 (1993).
 9. K. Yoshimori *et al.*, *J. Opt. Soc. Am. A* **14**, 3379 (1997).
 10. J. D. Armitage and A. Lohmann, *Opt. Acta* **12**, 185 (1965).
 11. F. Roddier, paper presented at the Proceedings of the

International Astronomical Union Colloquium, Sydney NSW, Australia, 1979.
 12. K. Itoh and Y. Ohtsuka, *J. Opt. Soc. Am. A* **3**, 94 (1986).
 13. K. Itoh *et al.*, *Jpn. J. Appl. Phys.* **29**, L1561 (1990).
 14. H. K. Tuy, *SIAM J. Appl. Math.* **43**, 546 (1983).
 15. L. A. Feldkamp *et al.*, *J. Opt. Soc. Am. A* **1**, 612 (1984).
 16. D. L. Marks *et al.*, *Appl. Opt.* **38**, 1332 (1999).
 17. Supported by the Defense Advanced Research Projects Agency. D.L.M. acknowledges the support of an NSF Graduate Fellowship.

16 February 1999; accepted 19 May 1999

Chiral Magnetic Domain Structures in Ultrathin FePd Films

H. A. Dürr,¹ E. Dudzik,^{1,2} S. S. Dhesi,¹ J. B. Goedkoop,³ G. van der Laan,^{1*} M. Belakhovsky,⁴ C. Mocuta,⁴ A. Marty,⁴ Y. Samson⁴

The magnetization profile of magnetically ordered patterns in ultrathin films was determined by circular dichroism in x-ray resonant magnetic scattering (CDXRMS). When this technique was applied to single crystalline iron palladium alloy layers, magnetic flux closure domains were found whose thickness can constitute a large fraction (~25 percent) of the total film.

X-ray reflections only occur when equivalent sites in a crystal are occupied by identical atoms. If the scattering amplitudes of equivalent sites are not the same, then forbidden reflections can occur. These are pronounced in the case of resonant diffraction, where virtual excitations from core to valence states impose the symmetry properties of the electronic and magnetic structure of the material (7). For instance, an antiferromagnetic ordering will give a magnetic superlattice with twice the size of the charge distribution. Here, we show how resonant magnetic scattering can be used to study complicated closure domain patterns (Fig. 1).

The domains display a left-right handedness known as chirality. It can be verified that the magnetization direction of each of the bulk domains in Fig. 1 is related to the magnetization of the closure domains right (left) above by a (counter)clockwise quarter-turn rotation in the yz plane. This extra symmetry condition should correspond to an additional Bragg condition, leading to an otherwise forbidden reflection. Although the possibility of measuring the long-period magnetic structure

by magnetic x-ray scattering was suggested by Blume in 1985 (2) and has been successfully applied to magnetic lattice periodicities on an atomic scale (3), we demonstrate here the case of magnetic domain structures. Using x-rays with circular polarization, we can make an unambiguous distinction between magnetic profiles with $\uparrow \rightarrow \downarrow \leftarrow \uparrow$ and $\uparrow \downarrow \uparrow \downarrow$ domain patterns because only the former has a chiral structure. The observation of circular dichroism in the x-ray resonant magnetic scattering (CDXRMS) signal, I —that is, its difference between left and right circularly polarized photons—allows us to recover the phase information that is generally lost in diffraction experiments. We demonstrate that this effect can be directly related to the magnetization profile in the film.

To observe the magnetization directions, we can use the equivalent in the x-ray region of either the Faraday rotation of linearly polarized light or the Kerr effect of elliptically polarized light. An increase in the sensitivity for the valence electron magnetization is obtained by tuning the photon energy to the Fe L_3 edge (wavelength $\lambda = 17.5 \text{ \AA}$), where a $2p$ core electron is excited into an empty, magnetically aligned $3d$ state. This wavelength is of the correct magnitude to be susceptible to the magnetic periodicity of the sample. The scattering signal measured in a diffraction experiment, $I \propto |\sum_n \exp(i\mathbf{q}\cdot\mathbf{r}_n) f_n|^2$ (where \mathbf{q} is the photon wave vector transferred in the scattering process), is the square of the modulus of the sum over all lattice sites, \mathbf{r}_n , of

the scattering amplitudes, f_n , weighted by a phase factor (4). Hannon *et al.* (5) showed that the resonant electrical dipole scattering amplitude can be written as

$$f_n = \hat{\mathbf{e}}' \cdot \hat{\mathbf{e}} F_n^{(0)} - i(\hat{\mathbf{e}}' \times \hat{\mathbf{e}}) \cdot \hat{\mathbf{M}}_n F_n^{(1)} + (\hat{\mathbf{e}}' \cdot \hat{\mathbf{M}}_n)(\hat{\mathbf{e}} \cdot \hat{\mathbf{M}}_n) F_n^{(2)} \quad (1)$$

where $\hat{\mathbf{e}}$ and $\hat{\mathbf{e}}'$ are the polarization vectors of the incident and scattered x-rays, respectively, and $\hat{\mathbf{M}}_n$ is the unit vector along the magnetization direction in the sample. The complex factors F_n describe the atomic resonant excitation and decay processes, and they can be expanded in terms of multipole moments of the ground state (6). The first term in Eq. 1 is due to scattering from the Fe charge distribution, whereas the latter two terms are purely magnetic scattering contributions. In the following we use the second term in Eq. 1 to reconstruct the magnetization profile of the film. The difficulty with this is that usually the absolute magnitude of the complex factors F_n is not very well known and can only be obtained directly under certain conditions, such as for multilayered samples (7, 8). However, the case of regular domain patterns results in an elegant way to separate the three scattering contributions in Eq. 1. The lateral domain periodicity leads to purely magnetic superstructure scattering peaks located symmetrically around the specularly reflected x-ray beam. For structurally well-ordered films with smooth interfaces, the charge scattering term in Eq. 1 contributes only to the specular peak. The two magnetic terms are linear and quadratic in $\hat{\mathbf{M}}_n$ and cause magnetic peaks at wave vectors $\pm\tau$ and $\pm 2\tau$, respectively ($2\pi/\tau$ is the domain periodicity) (3–5).

To assess the scattering from the individual domains in Fig. 1B, we must determine the scattering cross sections for the x-ray polarization components σ and π that are perpendicular and parallel to the scattering plane, respectively (9). For the scattering geometry used (Fig. 2A) and concentrating on the second term in Eq. 1, there are mainly two scattering paths producing π -polarized scattered light (4). For the bulk domains, $\hat{\mathbf{M}}_n$ is perpendicular to the film and σ -polarized incident radiation experiences a Faraday rota-

¹Daresbury Laboratory, Magnetic Spectroscopy Group, Warrington WA4 4AD, UK. ²University of York, York YO1 5DD, UK. ³University of Amsterdam, Valckenierstraat 65, NL 1018 XE Amsterdam, Netherlands. ⁴CEA/Grenoble, Service de Physique des Matériaux et Microstructures, 17 rue des Martyrs, 38054 Grenoble Cedex 9, France.

*To whom correspondence should be addressed. E-mail: g.vanderlaan@dl.ac.uk